Subcooled Flow Boiling of Carbon Dioxide Near the Critical Point Inside a Microchannel

Anatoly Parahovnik,* Mostafa Asadzadeh, Subith S. Vasu, and Yoav Peles
Department of Mechanical and Aerospace Engineering, University of Central Florida, Orlando, Florida 32816, USA

(Received 15 March 2020; revised 13 October 2020; accepted 14 October 2020; published 19 November 2020)

Subcooled flow boiling heat transfer of carbon dioxide (CO_2) at the microscale near the critical pressure is experimentally studied. The onset of nucleate boiling and the local heat-transfer coefficient are obtained under 26 experimental conditions, consisting of 17 sample points each, yielding 442 data points. Excess temperatures of about 1 K at the onset of nucleate boiling and heat-transfer coefficients of up to 200 kW/m^2 K are recorded. The heat-transfer coefficient and the onset of nucleate boiling models and correlations developed for low reduced pressures are compared to current experimental results. Modifications to these models are introduced to account for conditions pertinent to reduced pressures around unity. Overall, the correlations do not fully capture current measurements, suggesting that the physics of flow boiling heat transfer near the critical conditions exhibits some unique characteristics. Furthermore, it is observed that the experimentally obtained heat-transfer coefficient is better predicted by a model developed for flow boiling of CO_2. However, with increasing pressure, deviations between experiments and predictions increase.

DOI: 10.1103/PhysRevApplied.14.054050

I. INTRODUCTION

Carbon dioxide (CO_2) has long been used in various industries, such as the food and beverage industry, the oil and gas industry, and the manufacturing and construction industry. In its supercritical state, it has been recently studied as a potential fluid for Brayton power cycles. Concurrently, a century-long effort revealed many of the characteristics of flow boiling heat transfer under a range of flow and thermal conditions. Since early 2000, it has been researched at the microscale. However, thermal engineers have been reluctant to integrate microchannel flow boiling in their systems because of flow instabilities, the critical heat flux (CHF) condition, and inconsistencies between available correlations. Recent results [1] suggest that these issues can be resolved with CO_2, especially at reduced pressures close to unity. Nevertheless, besides a couple of studies at reduced pressures of up to 0.87 [2–6], not much is known about flow boiling heat-transfer characteristics under such conditions.

Flow boiling scientists seek to obtain data and reveal the underlining physics controlling the onset of nucleate boiling (ONB), two-phase heat-transfer coefficient (HTC), and CHF condition. Flow morphologies and a range of other effects, such as flow instabilities, have been meticulously documented and modeled. Frequently used models to predict ONB include Hsu's model [7], the Davis and Anderson model [8], and the Lienhard correlation [9]. Numerous correlations and models have been developed to predict the two-phase HTC. Several of the more notable ones include the Shah correlation [10], Kandlikar's correlation [11], and the Cheng correlation [6]. They were developed based on experimental results at lower reduced pressures and applied to boiling numbers that were, for the most part, below those pertinent to CO_2 near the critical condition.

Despite many years of research, flow boiling near the critical condition at the microscale has rarely been studied, and data pertinent to heat transfer are missing. Therefore, knowledge about the mechanisms controlling the heat-transfer process under such important conditions is lacking. This study seeks to address this shortcoming by providing experimental data about the onset of nucleate boiling and the heat-transfer coefficient of microscale flow boiling of carbon dioxide near its critical condition. A comparison with the correlations mentioned above that are developed for lower reduced pressures, lower boiling numbers, and larger channels is made in an attempt to assess their validity for CO_2 near the critical condition.

II. EXPERIMENTAL METHODS

A. Microfluidic device

The current microfluidic device is constructed from two substrates [Fig. 1(a)]. The 0.1 mm high and 2 mm wide microchannel is housed in the top 5-mm-thick piece, and

*tolik@knights.ucf.edu

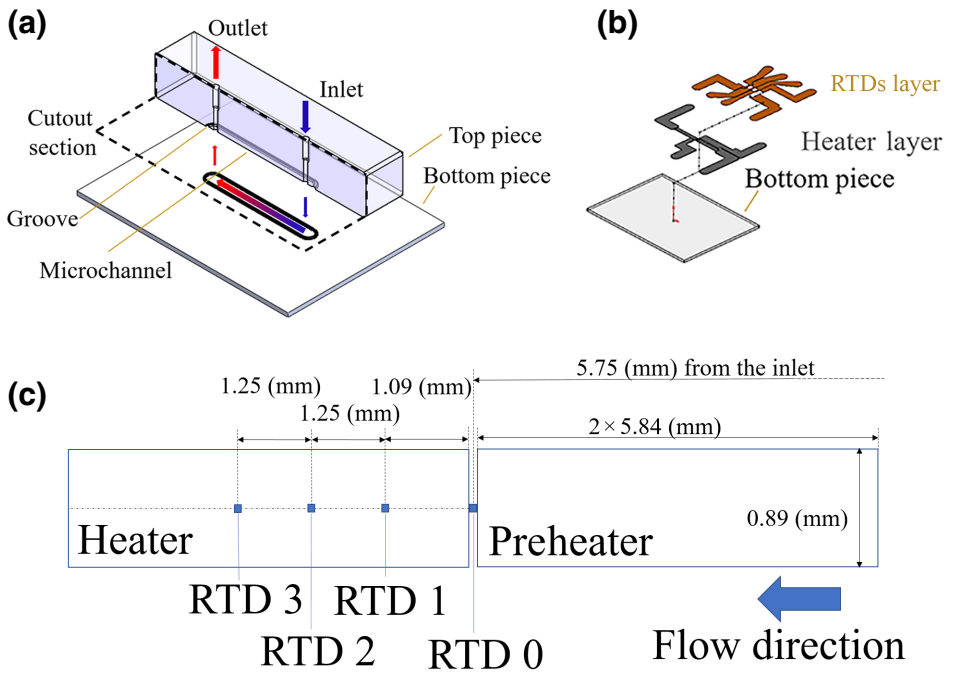

FIG. 1. Microfluidic device assembly. (a) Top and bottom fused silica pieces that form the microchannel and the inlet and exit manifolds. (b) The metallic layers that form the preheater, heater, and RTDs on the bottom piece. (c) The positions of the RTDs concerning the heater and preheater.

the bottom 500-μm-thick piece includes all electrical circuits. Fluid enters through the inlet port on the top piece, flows inside the microchannel, and exits through the outlet port. Metallic layers on the bottom piece's surface form a preheater, a heater, and four resistive temperature detectors (RTDs), as shown in Fig. 1(b). The top piece is made from fused silica to enable optical access to the flow inside the microchannel. The heater is placed 5.75 mm downstream from the inlet to ensure fully developed hydrodynamic flow. The RTDs are positioned according to the dimensions given in Fig. 1(c). Strength analysis is performed to ensure the device's structural integrity at the required operating pressures and is validated with the device pressurized to 1.5 times the designed operating pressure for 10 minutes (no fracture or leakage is detected during and after the test).

1. Microfabrication of the bottom piece

In the bottom piece's microfabrication process, titanium, platinum, and aluminum are deposited on top of the fused silica substrate to form the preheater and the heater. Photolithography processes transfer the design pattern onto the wafer. Subsequently, excess aluminum is removed using a wet etching process. Platinum and titanium are shaped using dry etching, and a 1.2 μm silicon oxide coating then insulates the heater and preheater. Similar microfabrication processes are repeated with different patterns to form the RTDs and their electrical connections. They are then covered with another silicon oxide layer for mechanical protection and electrical insulation. The upper silicon oxide layer is chemical-mechanically polished to enable intimate contact between the top and bottom pieces and prevent flow leakage. Next, the silicon dioxide layer is etched at the contact pad areas to allow electrical connectivity between the microdevice, the power supply, and the data acquisition unit. Finally, the wafer is cut into individual bottom pieces.

B. Experimental rig

1. Pneumatic setup and sampling setup

In the open-loop experimental setup (Fig. 2, left), CO_2 is delivered from a high-pressure tank at state 1 to a pressurizing vessel at state 2 through a filter, a check valve, and a three-way valve. This vessel, with a separating piston, allows control of the CO_2 pressure before it enters the microchannel. The pressure is regulated using nitrogen gas that resides on the piston's other side (state 3). When CO_2 at state 3 reaches the desired pressure, the three-way valve and the ball valve (state 4) are opened to allow flow through an external preheater (Q_1) before entering the microchannel through the package. Pressures at states 5 and 6 are measured using inlet and exit transducers made by Omega Engineering® (Model PX309-5KG5V). The exit pressure and the mass flow rate are controlled by two metering values (states 7 and 8). The metering valves have heating elements to prevent the solidification of CO_2 due to the Joule-Thomson (JT) effect. Before leaving the experimental setup to enter the ambient air, the flow rate is measured using a mass flow meter (state 9) made by Alicat® (Model M-20SLPM-D®).

The sampling setup consists of a microscope, a high-speed camera (Phantom® MIRO 310M®), a power

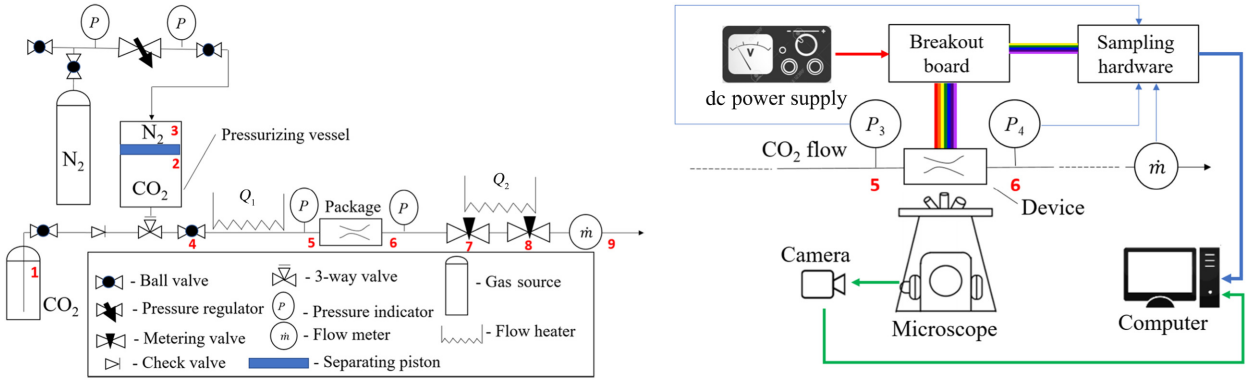

FIG. 2. Left: Schematic of the pneumatic experimental setup that enables independent control of the pressure and mass flow rate. Right: Schematic of the sampling setup consisting of a microscope, a high-speed camera, and a data acquisition system that synchronizes the images with transient surface temperature measurements.

supply (Kysight®, E3645A®), multimeters (Agilent®, 34410A®), a breakout board, and sampling hardware (National Instruments®, SCXI 1000®, and DAQ 9178®), which are connected to a computer (see Fig. 2, right). The sampling setup records synchronized images of the flow with temperature readings within the microchannel and applies the necessary heat load to the microfluidic device.

2. Package

A custom-made package connects the microfluidic device to the experimental rig and includes two main parts (see Fig. 3). The two-piece microdevice was sandwiched between a cover part (part 1) and the core part (part 2) that were fastened through six screws. Part 2 had a flow inlet and a flow outlet aligned with the microdevice's inlet and exit, respectively. It also includes two printed circuit boards (PCBs) with probe pins that connect the power supply to the heater and preheater and the RTDs to the data acquisition unit. (The probe pins are soldered to the PCBs on one end and are pressed against the microdevice's electrical pads on the other side.) Both parts are made of 316L stainless steel with a Mohs scale hardness of five, which is lower than that of fused silica with a Mohs hardness of seven, and a sufficiently high tensile strength of 205 MPa to support the required pressure. To avoid local stress concentrations, those surfaces that are in contact with the microfluidic device are polished. Structural analysis is performed to prevent damage from deflection during the assembly process.

C. Experimental procedure

Initially, the pressurizing vessel is filled with CO_2 to its full capacity. The valve between the CO_2 pressure tank and the pressuring tank is then closed, and the working pressure is set using a regulator that controls the N_2 pressure. Pressurized CO_2 is introduced into the device and, after a stabilization period, a leak test is performed by monitoring the pressure stability for another 2 minutes. The outlet ball valve is then opened, and the mass flow rate is set to desired values using the metering valves and the adjoining JT heater. Subsequently, the heat flux is increased in increments of 2–8 W/cm^2, depending on the mass flux. The hydraulic entrance length is estimated using the Reynolds number, Re, according to

$$Re = (GD_h)/\mu, \tag{1}$$

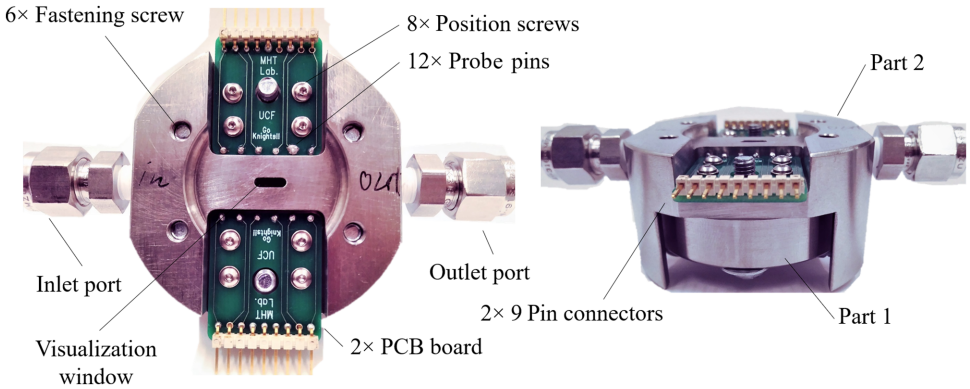

FIG. 3. Pictures of microfluidic device's package, consisting of two main parts. Part 1 supports the microdevice. Part 2 includes the fluidic ports, PCBs with electric probe pins, and a visualization window.

where G is the mass flux, D_h is the channel's hydraulic diameter, and μ is the dynamic viscosity at the inlet pressure and inlet temperature.

D. Data reduction and uncertainty analysis

Experimental data include the excess temperature, ΔT_{sat}, and the associated heat-transfer coefficient,

$$\Delta T_{\text{sat}} = T_w - T_{\text{sat}}, \tag{2a}$$

$$h = \frac{q'' - q''_{\text{loss}}}{\Delta T_{\text{sat}}}, \tag{2b}$$

where q and q_{loss} are the heat load and heat loss, respectively; T_w and T_{sat} are the wall and saturation temperatures, respectively.

Before conducting experiments, all RTDs are placed in an oven and calibrated over a temperature range of 297 to 373 K. A T-type thermocouple is used to measure the device temperature during the calibration process to relate the RTDs' electrical resistance to their respective temperatures. A linear curve fit between the resistances and temperatures is established and used during data processing.

The channel is vacuumed to assess heat losses. Heat is then applied to the heater, and the heat losses are estimated using a thermal resistance method, according to

$$q''_{\text{loss}} = (T_w - T_\infty)/R_{\text{thermal}}, \tag{3}$$

where T_w–T_∞ is the temperature difference between the wall (T_w) and the ambient temperature (T_∞). A thermal resistance, R_{thermal}, of 3.45 K/W, is found to predict the heat losses best. For each experimental data point, the heat loss is calculated and subtracted from the heat load. On average, the heat losses are estimated to be approximately 7%.

Experimental uncertainties are estimated using the propagation of uncertainty analysis [12]. The temperature uncertainty is estimated to be ± 0.33 K, and the pressure uncertainty is estimated to be ± 0.017 MPa. The mass flow rate's uncertainty is estimated to be ± 0.1 slpm, leading to an uncertainty of ± 10 kg/m^2 s in the mass flux. Consequently, the uncertainty of the boiling number is estimated to be $\pm 10\%$.

III. SUBCOOLED FLOW BOILING MODELS

Experiments are compared to several established ONB and HTC correlations. Modifications to these correlations are also considered and analyzed. The experiments seek to obtain the onset of subcooled nucleate flow boiling and the heat-transfer coefficient at low void fractions.

A. The onset of nucleate boiling

The following three established models are considered to supplement the experiments: Hsu's model [7], the Davis and Anderson model [8] with and without adjustments, and an experimentally based correlation proposed by Lienhard [9].

Two adjustments to the Davis and Anderson model are introduced. A generalized gas equation of state (GEOS), $Pv = ZRT$, is used instead of the ideal gas law. The Kelvin equation [13] and the Clausius-Clapeyron equation are used to reformulate the original model. As a result, the following two constants are altered to

$$a = a_{\text{GEOS}} = \frac{2\sigma}{P_l}\left(1 - \frac{z_l}{z_g}\right) \quad \text{and} \quad c = c_{\text{GEOS}} = \frac{R_{\text{CO}_2}(z_l - z_g)T_{\text{sat}}}{h_{fg}}, \tag{4}$$

where Z_l and Z_g are the compressibility factors of the liquid and gas phases, respectively; σ is the surface tension; P_l is the liquid pressure; and h_{fg} is the latent heat of vaporization.

The second change included the integration of the boundary layer theory [14], which resulted in a modified temperature profile that produced the following equations:

$$\frac{T_w - T_l}{T_w - T_\infty} = \left(\frac{y}{2\delta_T}\right)\left[3 - \left(\frac{y}{\delta_T}\right)^2\right], \tag{5}$$

where for the calculation of the thermal boundary layer, δ_T, Eqs. (6)–(8) are used.

$$\delta_{\text{hyd}} = 4.92 x Re_x^{-\frac{1}{2}}, \tag{6}$$

$$\delta_{\text{hyd}} = 0.37 x Re_x^{-\frac{1}{5}}, \tag{7}$$

$$\Delta = 0.976 P_r^{-\frac{1}{3}}\left[1 - \left(1 - \frac{x_0}{x}\right)^{\frac{3}{4}}\right]^{\frac{1}{3}}, \tag{8a}$$

$$\delta_T = \Delta \cdot \delta_{\text{hyd}}. \tag{8b}$$

where δ_{hyd} is the hydrodynamic boundary layer thickness, x is the distance from the inlet, Re_x is the local Reynolds number, x_0 is the unheated distance from the entrance, y is the perpendicular distance from the wall, and Δ is the ratio between the thermal and the hydrodynamic boundary layers.

B. Heat-transfer coefficient

The Shah correlation [10] for low subcooled conditions [i.e., $(T_{\text{sat}} - T_b)/(T_w - T_{\text{sat}}) < 2$] is divided into two

dimensionless parameters:

$$\psi = 230B_o^{0.5}, \quad B_o > 0.3 \times 10^{-4}, \tag{9a}$$

$$\psi = 1 + 46B_o^{0.5}, \quad B_o < 0.3 \times 10^{-4}, \tag{9b}$$

$$\psi = \frac{q''}{(T_w - T_{\text{sat}})h_L}, B_o = \frac{q''}{Gh_{fg}},$$

where B_o is the boiling number and ψ is a dimensionless heat-transfer coefficient ratio that is normalized using the Dittus-Boelter correlation [15] for the single-phase heat-transfer coefficient, h_L, and T_b is the fluid bulk temperature. For large subcooled temperatures [i.e., $(T_{\text{sat}}-T_b)/(T_w-T_{\text{sat}}) \geq 2$], $(T_{\text{sat}}-T_b)/(T_w-T_{\text{sat}})$ is added to Eqs. (9a) and (9b) as follows:

$$\psi = 230B_o^{0.5} + \frac{T_{\text{sat}} - T_b}{T_w - T_{\text{sat}}}, \quad B_o > 0.3 \times 10^{-4}, \tag{10a}$$

$$\psi = 1 + 46B_o^{0.5} + \frac{T_{\text{sat}} - T_b}{T_w - T_{\text{sat}}}, \quad B_o < 0.3 \times 10^{-4}, \tag{10b}$$

the Kandlikar correlation [16] for subcooled flow boiling is as follows:

$$\psi = 1058B_o^{0.7}F_{\text{fl}}, \tag{11}$$

the Gnilinski [17] correlation is used to calculate the single-phase heat-transfer coefficient, and the B_o number is defined in the same manner as that in the Shah correlation. The coefficient, F_{fl}, depends on the type of fluid, and, for CO_2, Ducoulombier *et al.* [5] stated that a value of 2.1 should be used.

Finally, the Cheng correlation [6] relates the heat-transfer coefficient to the reduced pressure, the molar mass, and the heat flux according to

$$h = 131P_r^{-0.0063}(-\log_{10}P_r)^{-0.55}M^{-0.55}(q'')^{0.58}, \tag{12}$$

$$\psi = \frac{h}{h_L}, \tag{13}$$

where P_r is the reduced pressure and M is the molar mass.

IV. RESULTS AND DISCUSSION

Twenty-six experimental conditions are studied (at different mass fluxes), each consisting of 17 samples (for various heat fluxes) for a total of 442 data points. Independent variables include pressure, mass flux, heat flux, and channel orientation (i.e., the heated surface either faces up or down, but mostly faces down). Dependent variables include local surface temperatures, ONB, and HTC. The pressure ranges from 6 to 6.91 MPa, resulting in reduced pressures ranging from 0.82 to 0.95. The mass flux varies between 148.1 and 1703.7 kg/m^2 s, whereas most of the data points are concentrated around 160, 550, and 1550 kg/m^2 s. A heat flux of up to 55 W/cm^2 is applied.

A. Boiling curves

Figure 4 depicts boiling curves at three different pressures. At low heat fluxes, a single-phase liquid flow is observed, in which the temperature difference is a function of the location, as expected for a constant heat-flux boundary condition. Following the onset of nucleate boiling, the local surface temperatures gradually converge, suggesting a transition to fully developed nucleate flow boiling. In fully developed nucleate flow boiling, the heat-transfer process is dominated by the generation of bubbles and the associated latent heat transfer, rather than by forced convective processes. As a result, it is less dependent on mass flux. Thus, curves for different mass fluxes tend to

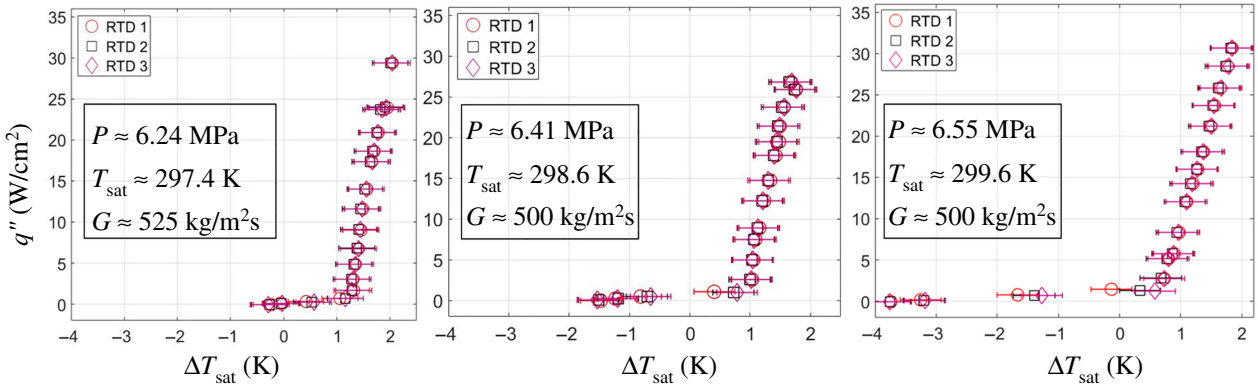

FIG. 4. Boiling curves for pressures of 6.24, 6.41, and 6.55 MPa. Low superheated temperatures at ONB of 1.2, 0.82, and 0.64 K, respectively, are observed. All curves are steep for post-ONB conditions, indicating high heat-transfer coefficients during flow boiling. Once boiling is fully developed, the three RTDs register almost the same temperatures, suggesting the heat-transfer process is dominated by nucleate flow boiling.

converge. The onset of nucleate boiling is recorded at superheated temperatures (ΔT_{ONB}) of 1.2, 0.82, and 0.64 K for pressures of 6.24, 6.41, and 6.55 MPa, respectively.

B. The onset of nucleate boiling

The superheated temperature at the onset of nucleate boiling is determined through the intersection of two linearly fitted curves: one for single-phase liquid data and one for flow boiling data. The superheated temperatures at the local onset of nucleate boiling (i.e., once boiling is initiated at a particular location) are inferred for each RTD separately. It is found that the deviations are about one fourth of the measurement uncertainty. Thus, it is concluded that the local onset of nucleate boiling is independent of position, at least under the conditions considered in this study.

As shown in Fig. 5, a peak value of $\Delta T_{ONB} = 1.6$ K is observed at the lowest pressure, which gradually diminishes as the pressure approaches the critical condition. The dependencies of pressure and mass flux on ΔT_{ONB} are evaluated using the Pearson correlation coefficient [18], which identifies dependencies between the superheated temperature and the mass flux and between the superheated temperature and pressure. Values of 0.06 and -0.94 are obtained for the relation of ΔT_{ONB}-G and ΔT_{ONB}-P, respectively. (A value of one suggests perfect linear dependency, a value of zero means no dependence, and a negative value corresponds to an inverse dependency.) Thus, ΔT_{ONB} strongly depends on pressure, but not on mass flux. The effect of the orientation is within the uncertainty level, and therefore, is indistinguishable.

The Lienhard correlation [9] assumes homogenous bubble nucleation, as opposed to heterogeneous nucleation. Under this assumption, the onset of nucleate boiling occurs only at the molecular level, when the fluid attains a temperature higher than that of the corresponding metastable state. Therefore, the correlation provides an upper bound for the superheated temperature required for boiling inception. In engineered systems, homogenous nucleation cannot be practically implemented and boiling is initiated by heterogeneous nucleation, corresponding to a lower superheated temperature, as observed in the current experimental study.

On the other hand, the Davis and Anderson model assumes a wide range of active cavity sizes, and thus, provides a lower bound for the onset of nucleate boiling. The heated surface used in the experiments is polished. Therefore, it has a limited range of cavities to initiate bubble nucleation, leading to higher superheated temperatures than those predicted by the Davis and Anderson model.

Figure 5 also shows that most of the theoretical calculations are unable to predict the experimental results, whether it is an empirical correlation (i.e., Lienhard's correlation) or theoretically derived models (i.e., those of Hsu and Davis and Anderson). The Lienhard correlation overpredicts all experimental results with a mean average error (MAE) of 259%, but captures the observed trend. MAEs of 83.2%, 88.1%, 80%, and 85% are calculated for the Davis and Anderson model [8], with the adjusted equation of state (EOS) (i.e., $pv = zRT$), with the Frost and Dzackovic coefficient [19], and with a boundary layer (BL) integrated profile, respectively. The Davis and Anderson model with adjusted EOS best captures the physical phenomena and should be examined in the future for heated surfaces with a broad range of cavity sizes.

Hsu's model predicts the onset of nucleate boiling on a heated surface based on the presence of cavities within a specific size range. The hyperbolic curves in Fig. 6 represent the calculated active cavities range for pressures of 6, 6.51, and 6.91 MPa. The upper branch, marked with a red line, sets the upper limit of the active cavity sizes, and the lower branch, marked with a blue line, sets the lower limit.

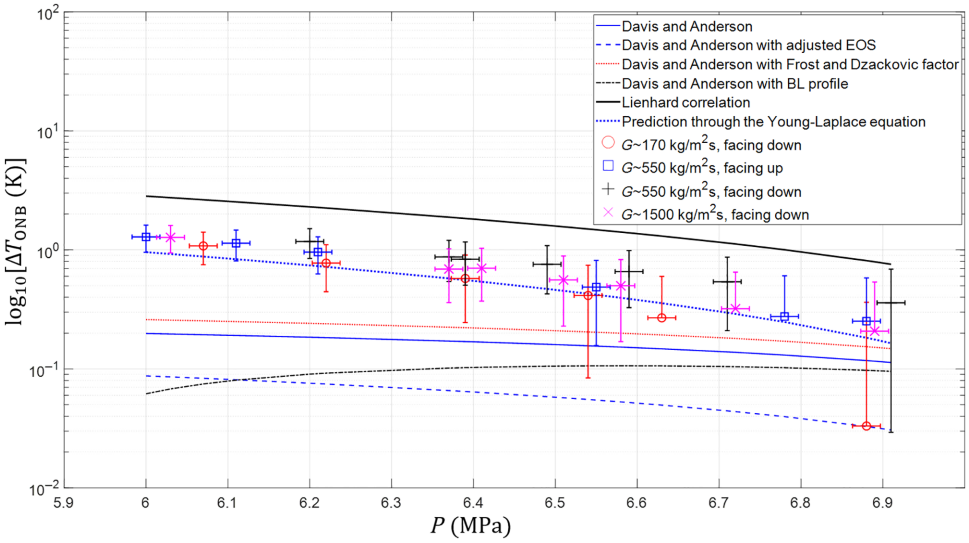

FIG. 5. Experimentally obtained excess temperature at the onset of nucleate boiling along with predictions of several models. ΔT_{ONB} values are much lower than those typically reported at low reduced pressures, and they tend to diminish with pressure.

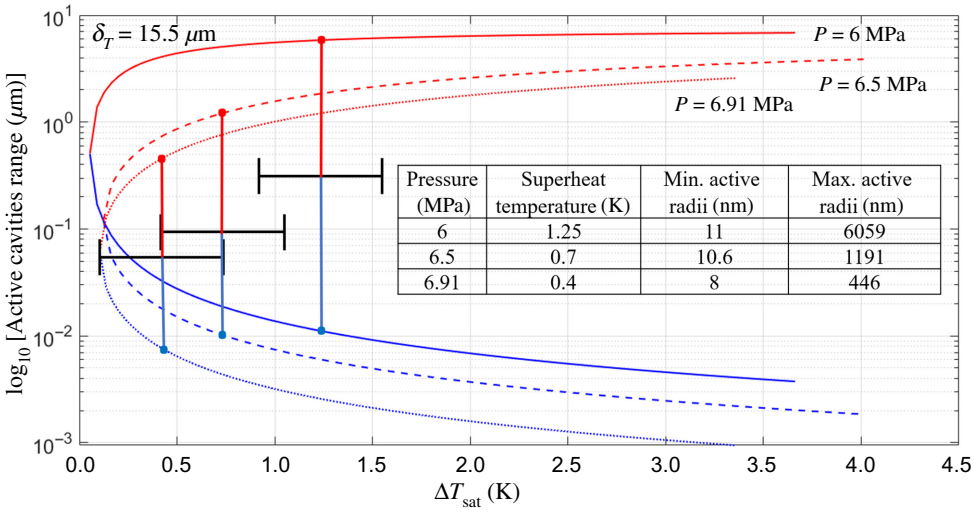

Pressure (MPa)	Superheat temperature (K)	Min. active radii (nm)	Max. active radii (nm)
6	1.25	11	6059
6.5	0.7	10.6	1191
6.91	0.4	8	446

FIG. 6. Range of active nucleation sites for three pressures studied based on Hsu's model. Three experimental results with their error bars, depicted as horizontal black lines, are superimposed on the corresponding curves generated based on Hsu's model. Vertical lines are sketched from these data points, and the intersection with the curves, marked with dots, provides the lower range and upper range of active nucleation sites. (Notably, these data points' vertical positions are placed arbitrarily in the middle between the upper and lower curves.) Size of the active cavities reduces with pressure. Thus, surface excess temperature at ONB is expected to decrease at higher pressures for smooth surfaces with only nanoscale cavities.

When the surface has cavities between these two curves, bubble nucleation occurs. The crosses inside the hyperbolic curves are the measured ΔT_{ONB} values for the three corresponding pressures. The limiting values for the upper and lower intersection points, marked with large dots on the hyperbolic curves, are explicitly mentioned Fig. 6.

According to Hsu's model, the effect of pressure on ΔT_{ONB} is better understood when considering the size range of active nucleation sites shown in Fig. 6. The size of the active cavities decreases with pressure, which is apparent from the three curves' downward shifts. Thus, excess temperature at the onset of nucleate boiling on surfaces with only large cavities (larger than several microns) increases with pressure. Simultaneously, it decreases for smooth surfaces with only cavities at the nanoscale or smaller. In other words, for rough surfaces, ΔT_{ONB} is expected to increase with pressure and, on smooth surfaces, such as the one in the current study, it is expected to decrease.

For the experimentally obtained ΔT_{ONB} values, Hsu's model predicts active radii in the range of 11–6059, 10.6–1191, and 8.0–446 nm for pressures of 6, 6.5, and 6.91 MPa, respectively, which are marked by the six dots on the three curves. Since bubble nucleation will occur only if the surface has cavities in that range, it is interesting to determine if the onset of nucleate boiling is triggered by larger cavities or smaller ones. To answer this question, one needs to estimate the size and type of surface cavities.

The microfluidic device's surface roughness is measured to be 150 nm, so it is evident that large cavities do not trigger the onset of nucleate boiling. Furthermore, due to the low surface tension of CO_2, these cavities are partially flooded, and therefore, produce much smaller effective nucleation sites [20]. Thus, it can be concluded that cavities initiating the onset of nucleate boiling are at the lower spectrum of the active cavity sizes, corresponding to the lower three curves in Fig. 6. Furthermore, the effective cavity size in the current heated surface is estimated to be about 10 nm, corresponding to the smallest active cavities calculated by Hsu's model, as shown in Fig. 6. If the cavities have the same geometry as those discussed by Hsu, the cavity size leads to a nominal bubble radius of 12.5 nm. Excess temperature at the onset of nucleate boiling can now be independently estimated from the Young-Laplace equation [21],

$$P_{\text{eff}} = P_f + \frac{2\sigma}{r_{\text{bubble}}}, \tag{14}$$

and compared with the corresponding values obtained experimentally. (P_{eff} is the pressure inside the bubble, P_f is the surrounding pressure, and r_{bubble} is the bubble radius of curvature.) The lowest active cavity size predicted by Hsu's model is substituted into the Young-Laplace equation as the corresponding radius of curvature. With a known radius and a known surface tension, the pressure difference between the vapor inside the bubble and the liquid outside is directly obtained. Since the liquid pressure is known, the pressure inside the bubble is inferred. Subsequently, the saturation temperature is obtained from the thermodynamic equation of state [22] based on the calculated vapor pressure. The difference between the saturated

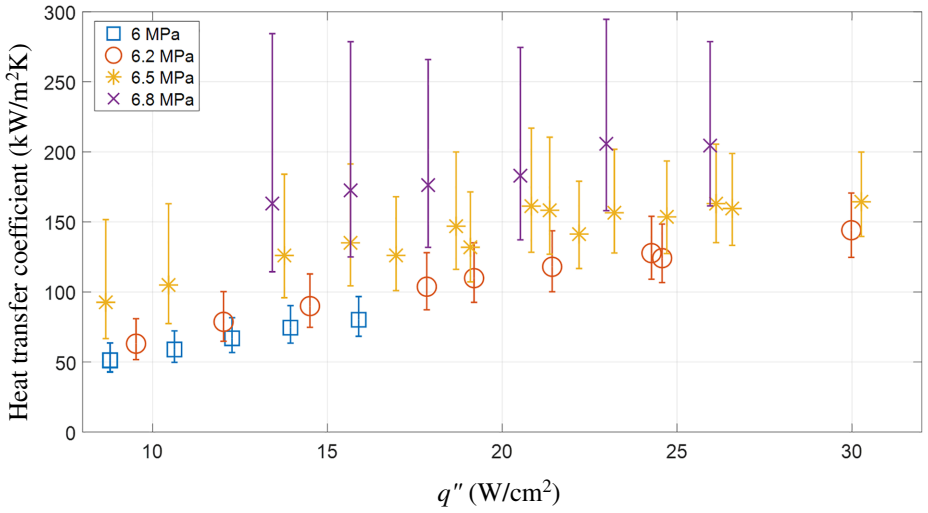

FIG. 7. Heat-transfer coefficient for mass flux of 420–600 kg/m^2 s at RTD 3. Average values range from 51.2 to 204.5 kW/m^2 K and mainly depend on pressure. Excess temperature during boiling ranges from 0.4 to 3 K, while the surface temperature uncertainty is ±0.33 K, leading to large uncertainties in the heat-transfer coefficients.

vapor temperature inside the bubble and the surrounding liquid saturation temperature provide the superheated temperature required for the onset of nucleate boiling. Once the surface temperature is determined, the superheated temperature corresponding to P_f can be obtained and used for comparison with experimental results (i.e., the excess temperature is the difference between the saturation temperature at P_{eff} and the saturation temperature at P_f). As shown in Fig. 5 by the curve termed "predictions from the Young-Laplace equation," the results are within the uncertainty measurement of the surface temperature. The Young-Laplace equation is a simplified version of the Davis and Anderson model, where the fluid adjoined to the wall is assumed to have a uniform temperature equal to the surface temperature. This assumption holds for the current study due to the small nuclei bubbles produced on top of the polished surface.

To conclude, the lowest active cavity size predicted by Hsu's model is used in combination with the Young-Laplace equation to predict best the superheated temperatures required for the onset of nucleate boiling on a polished surface inside a microchannel.

C. Heat-transfer coefficient

Figure 7 shows that the local heat-transfer coefficient for RTD3 has values of 51.2–204.5 kW/m^2 K. It appears that the heat-transfer coefficient is proportional to the heat flux and inversely proportional to the mass flux. This conclusion agrees with the flow boiling heat-transfer coefficient correlations because the boiling number is proportional to the heat flux.

The boiling number in this study reaches a value of 5×10^{-3}, while the Shah correlation is developed based on experimental data with boiling numbers up to 10^{-3}. The heat-transfer coefficients are normalized using the single-phase Dittus-Boelter correlation to examine the fit of the

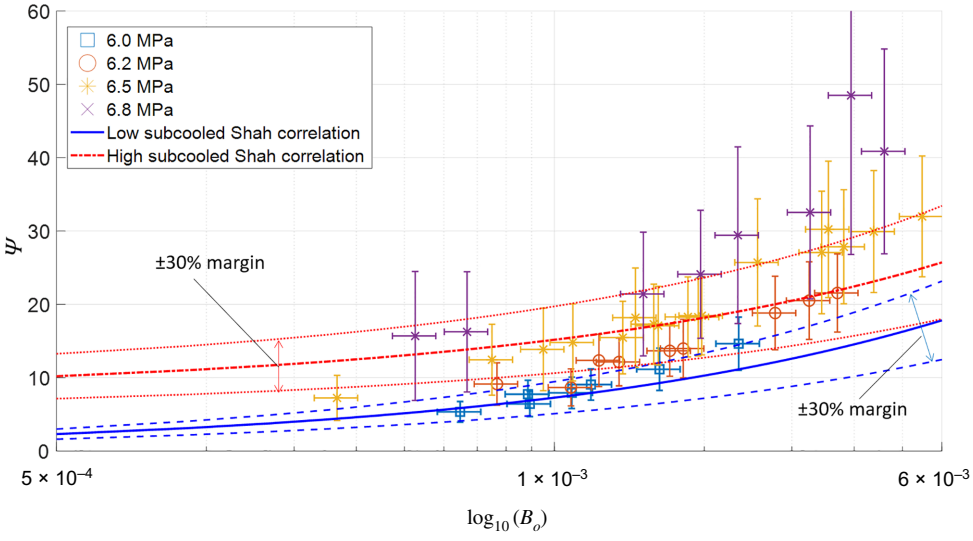

FIG. 8. Comparison of experimentally obtained dimensionless two-phase heat-transfer coefficient with the Shah correlation. Correlation reasonably predicts the heat-transfer coefficient at a low pressure of 6 MPa, corresponding to relatively low boiling numbers, but underpredicts experiments at higher pressures, corresponding to higher boiling numbers.

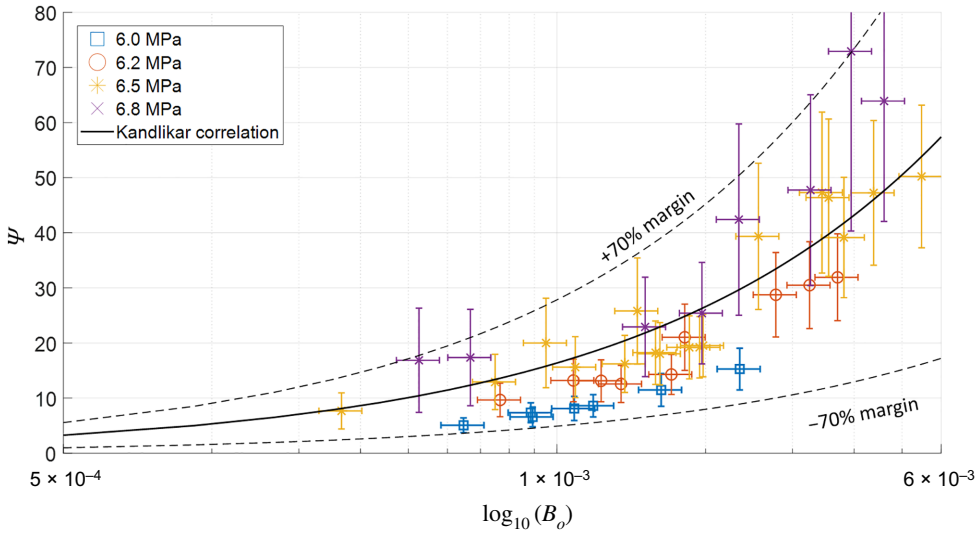

FIG. 9. Comparison of experimentally obtained dimensionless two-phase heat-transfer coefficient with the Kandlikar's correlation. Correlation reasonably predicts experimental data with an overall MAE of 24.3%.

correlations to experimental data [15]. This normalization allows a direct comparison of experimentally obtained HTC values with Shah's dimensionless heat-transfer coefficient ratio, ψ. For a pressure of 6.0 MPa with a maximum boiling number of 2.5×10^{-3}, the results agree with the correlation within a margin of $\pm 30\%$ (see Fig. 8). However, with increasing pressure, Shah's correlation gradually underpredicts the experimental results. Likewise, experimental measurements progressively diverge from the correlation with increasing boiling number. Thus, the Shah correlation is unable to predict experiments outside the original boiling number range.

Figure 9 compares experimental data to the Kandlikar correlation [11] with a correction coefficient, F_{fl}, of 1.984. The coefficient is obtained by a curve-fitting process that minimizes the MAE between experiments and the correlation. Regardless, it is in good agreement with the coefficient of 2.1 suggested by Ducoulombier *et al.* [5]. As a general rule, the correlation predicts higher ψ compared with those of Shah's correlation. Both the Shah correlation and the Kandlikar correlation show similar trends due to the boiling number power law used to predict ψ (0.5 and 0.7, respectively). Kandlikar's correlation best predicts data for 6.5 MPa, whereas it overpredicts the results for lower pressures of 6 and 6.2 MPa; the highest pressure of 6.8 MPa is underpredicted. Regardless, the entire data set falls within a $\pm$ 70% band with a MAE of 24.3%.

If each experimental curve at a specific pressure is fitted independently, F_{fl} coefficients of 0.9457, 1.51, 1.936, and 2.686 for pressures of 6, 6.2, 6.5, and 6.8 MPa, respectively, are produced. Appling F_{fl} coefficients results in a MAE of 15% and encompasses data for each pressure within a $\pm 30\%$ margin band.

For a minimal MAE, the coefficient is linearly fitted to the reduced pressure, according to Eq. (15), with an R^2 of 0.986:

$$F_{\mathrm{fl}} = 15.35 P_r - 11.5, \tag{15}$$

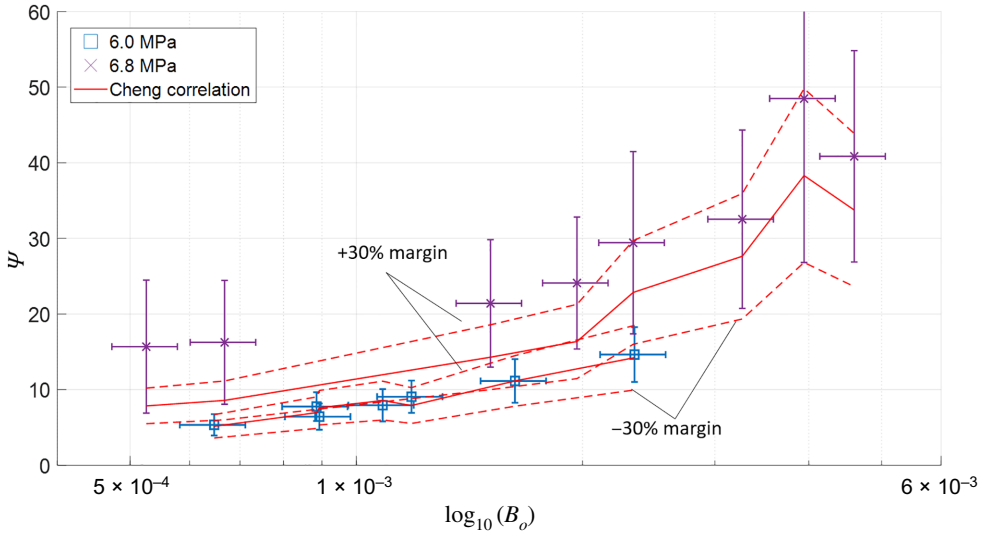

FIG. 10. Comparison of experimentally obtained dimensionless two-phase heat-transfer coefficient with the Cheng correlation. Correlation predicts experimental data well with a MAE of 19.2%.

at the critical pressure, Eq. (15) provides a value of 3.85, which is within the expected range reported by Kandlikar [11]. For low reduced pressures, Eq. (15) leads to negative values, and therefore, this linear approximation should be limited to reduced pressures larger than 0.8.

The Cheng correlation matches experimental results with a MAE of 19.2% for the entire data set. For the 6.0 MPa experiments (reduced pressure of 0.81), the correlation with its margins (±30%) coincide with experimental data (see Fig. 10). For 6.8 MPa (reduced pressure of 0.93), due to small temperature differences, the uncertainty of experimental data is considerably larger and still within the correlated results. However, the correlation gradually deviates from experimental results as the critical pressure approaches unity, such that MAEs of 7.9%, 15.4%, 23.4%, and 29.8% for pressures of 6, 6.2, 6.5, and 6.8 MPa, respectively, are recorded.

To conclude, Shah's and Kandlikar's correlations are formulated using experimental data for a wide range of fluids. Since the Cheng correlation is derived based on conditions closest to those used in the current study, it is not entirely surprising that it best predicts experimental results. Nevertheless, at reduced pressures above 0.87, Chang's correlation presents significant discrepancies to experimental results.

V. CONCLUSIONS

In this work, experimental capabilities reveal a significant enhancement in heat transfer with flow boiling of CO_2 near the critical point at the microscale. A low superheated temperature and high heat-transfer coefficients are reported in the present study. Several analytical models complement current experiments and are used to infer the active cavity size. It is found that the superheated temperature at the onset of nucleate boiling is inversely proportional to the operating pressure, which can be attributed to the reduction of the active cavity size required for the onset of nucleate boiling. No dependency between the superheated temperature at the onset of nucleate boiling and mass flux is observed.

The proposed corrections to Davis and Anderson's model do not better predict the current experimental data, despite the added computational complexity. Experimental results of the onset of nucleate boiling are confined within the analytical models and the empirical correlation. Fixing the active nuclei bubble size derived from Hsu's model, applying it to the Young-Laplace equation, and calculating the saturation temperature for the effective pressure result in good agreement with current experiments.

Heat-transfer coefficients of 51.2–204.5 $kW/m^2\,K$ are experimentally obtained, and no dependency on the mass flux is established. It is found that Shah's correlation underpredicts experiments for reduced pressures above 0.81. Kandlikar's correlation predicts experiments within a margin of ±30% and a MAE of 15% with an adjusted coefficient. The Cheng correlation matches experimental data best, although the error increases as the reduced pressure approaches unity.

The discrepancies between correlations and experimental results are linked to the high reduced pressure used to obtain experimental data (from 0.82 to 0.95 compared with less than 0.76, less than 0.8, and less than 0.87 for Shah's, Kandlikar's, and Cheng's correlations, respectively). Furthermore, the Shah and Kandlikar correlations are developed using a large number of fluids, and thus, can be more generally applied, but with a somewhat compromised accuracy.

ACKNOWLEDGMENTS

This work is funded mainly by the Office of Naval Research (ONR) under Grant No. N00014-18-1-2362 with Dr. Mark Spector as the program manager and the Israel Ministry of Defense (IMOD). The authors would like to acknowledge the Cornell NanoScale Science & Technology Facility (CNF) for staff support, help, and use of facilities in the fabrication of the microdevices. The CNF is a member of the National Nanotechnology Coordinated Infrastructure (NNCI), which is supported by the National Science Foundation.

[1] D. Hellenschmidt, M. Bomben, G. Calderini, M. Boscardin, M. Crivellari, S. Ronchin, and P. Petagna, New insights on boiling carbon dioxide flow in mini- and micro-channels for optimal silicon detector cooling, Nucl. Instrum. Methods Phys. Res. Sec. A **958**, 162535 (2020).

[2] J. R. Thome and J. El Hajal, Flow boiling heat transfer to carbon dioxide: General prediction method, Int. J. Refrig. **27**, 294 (2004).

[3] L. Cheng, G. Ribatski, L. Wojtan, and J. R. Thome, New flow boiling heat transfer model and flow pattern Map for carbon dioxide evaporating inside horizontal tubes, Int. J. Heat Mass Transfer **49**, 4082 (2006).

[4] M. Ducoulombier, S. Colasson, J. Bonjour, and P. Haberschill, Carbon dioxide flow boiling in a single microchannel – part I: Pressure drops, Exp. Therm. Fluid Sci. **35**, 581 (2011).

[5] M. Ducoulombier, S. Colasson, J. Bonjour, and P. Haberschill, Carbon dioxide flow boiling in a single microchannel – part II: Heat transfer, Exp. Therm. Fluid Sci. **35**, 597 (2011).

[6] L. Cheng, G. Ribatski, and J. R. Thome, New prediction methods for CO_2 evaporation inside tubes: Part II—An updated general flow boiling heat transfer model based on flow patterns, Int. J. Heat Mass Transfer **51**, 125 (2008).

[7] Y. Y. Hsu, On the size range of active nucleation cavities on a heating surface, J. Heat Transfer **84**, 207 (1962).

[8] E. J. Davis and G. H. Anderson, The incipience of nucleate boiling in forced convection flow, AIChE J. **12**, 774 (1966).

[9] J. H. Lienhard, Correlation for the limiting liquid superheat, Chem. Eng. Sci. **31**, 847 (1976).

[10] M. Mohammad Shah, A general correlation for heat transfer during subcooled boiling in pipes and annuli, ASHRE Trans. **83**, 202 (1977).
[11] S. G. Kandlikar, A general correlation for saturated Two-phase flow boiling heat transfer inside horizontal and vertical tubes, J. Heat Transfer **112**, 219 (1990).
[12] R. J. Moffat, Describing the uncertainties in experimental results, Exp. Therm. Fluid Sci. **1**, 3 (1988).
[13] K. P. Galvin, A conceptually simple derivation of the kelvin equation, Chem. Eng. Sci. **60**, 4659 (2005).
[14] A. Bejan, *Convection Heat Transfer*, 4th Edition (Wiley, New York, 2013).
[15] T. L. Bergman, A. S. Lavine, F. P. Incropera, and D. P. DeWitt, *Fundamentals of Heat and Mass Transfer* (Wiley, Chichester, 2011).
[16] S. G. Kandlikar, Heat transfer characteristics in partial boiling, fully developed boiling, and significant void flow regions of subcooled flow boiling, ASME. J. Heat Transfer. **120**, 395 (1998).
[17] V. V. Gnielinski, in Neue Gleichungen Fiir den Wiirme- und den Stoffiibergang in Turbulent DurchstrSmten Rohren und Kan/Ilen (1975), p. 9.
[18] J. Benesty, J. Chen, Y. Huang, and I. Cohen, in *Pearson Correlation Coefficient, Noise Reduction in Speech Processing*, edited by I. Cohen, Y. Huang, J. Chen, J. Benesty (Springer, Berlin, Heidelberg, 2009), pp. 1–4.
[19] J. G. Collier and J. R. Thome, *Convective Boiling and Condensation* (Clarendon Press, Oxford, 1994).
[20] A. E. Bergles and S. G. Kandlikar, On the nature of critical heat flux in microchannels, J. Heat Transfer **127**, 101 (2005).
[21] P. Atkins and J. De Paula, *Physical Chemistry*, 8th Edition (Oxford University Press, New York, 2006).
[22] R. Span and W. Wagner, A New equation of state for carbon dioxide covering the fluid region from the triple-point temperature to 1100 K at pressures up to 800 MPa, J. Phys. Chem. Ref. Data **25**, 1509 (1996).